A Theoretical Model Study of the Influence of Fluid Stresses on a Cell Adhering to a Microchannel Wall

Donald P. Gaver, III, and Stephanie M. Kute
Department of Biomedical Engineering, Tulane University, New Orleans, Louisiana 70118 USA

ABSTRACT We predict the amplification of mechanical stress, force, and torque on an adherent cell due to flow within a narrow microchannel. We model this system as a semicircular bulge on a microchannel wall, with pressure-driven flow. This two-dimensional model is solved computationally by the boundary element method. Algebraic expressions are developed by using forms suggested by lubrication theory that can be used simply and accurately to predict the fluid stress, force, and torque based upon the fluid viscosity, μ, channel height, H, cell size, R, and flow rate per unit width, $Q_{2\text{-}d}$. This study shows that even for the smallest cells ($\gamma = R/H \ll 1$), the stress, force, and torque can be significantly greater than that predicted based on flow in a cell-free system. Increased flow resistance and fluid stress amplification occur with bigger cells ($\gamma > 0.25$), because of constraints by the channel wall. In these cases we find that the shear stress amplification is proportional to $Q_{2\text{-}d}(1 - \gamma)^{-2}$, and the force and torque are proportional to $Q_{2\text{-}d}(1 - \gamma^2)^{-5/2}$. Finally, we predict the fluid mechanical influence on three-dimensional immersed objects. These algebraic expressions have an accuracy of ~10% for flow in channels and thus are useful for the analysis of cells in flow chambers. For cell adhesion in tubes, the approximations are accurate to ~25% when $\gamma > 0.5$. These calculations may thus be used to simply predict fluid mechanical interactions with cells in these constrained settings. Furthermore, the modeling approach may be useful in understanding more complex systems that include cell deformability and cell-cell interactions.

INTRODUCTION

Cells in nature frequently adhere to the walls of channels or tubes whose cross-sectional dimensions are similar to those of the cells themselves. This can occur in situations as varied as leukocyte adhesion in the vascular system to biofilm formation in porous media. Fluid flowing through these systems exerts stresses on these cells, which may influence their adhesion to the microchannel wall. In addition, cell adhesion can greatly influence the flow field within these channels. To fully understand the interrelationships between cell behavior and flow, a fundamental understanding of the modification of the flow-field within the channel, the flow-induced stress, force, and torque on the cell body is necessary. Several specific lines of research that can benefit from improved understanding of the hydrodynamic interaction between a cell and the environment it inhabits are described below.

Leukocyte adhesion

Much is already known about the adhesion process with leukocytes, particularly neutrophils. Briefly, the adhesion process is initiated by an inflammation response, which results in vascular endothelial cells displaying specific adhesion molecules that bind to convecting neutrophils. The initial attachment is mediated by adhesion molecules known as selectins, which slow the neutrophils and cause them to roll along the endothelial surface. Next, neutrophil activation ensues, resulting in the up-regulation of the integrin family of adhesion molecules, which initiates firm contact between the endothelium and neutrophil. Subsequently, the neutrophil flattens and eventually migrates between inter-endothelial junctions to enter the tissue.

Clearly the strength and rate of attachment of the ligand-receptor bindings are key determinants of the adhesion process, and for this reason they are the focus of many studies (for example, Goetz et al., 1994; Hammer and Apte, 1992; Konstantopoulos and McIntire, 1996; Tempelman and Hammer, 1994). Olivier and Truskey (Olivier and Truskey, 1993) have examined the force and torque associated with shape changes during sequestration, and predicted that a significant reduction in stress and torque would occur. However, an unstudied aspect of the above investigations relates to the fluid mechanical interaction that occurs during the adhesion and sequestration of cells in small vessels (for example, postcapillary venules) wherein a cell, or a cluster of cells, may cause significant flow disruption and thus increase the stress exerted on the cell. A goal of the research described herein is to identify the scenarios in which such flow disruption may be significant, and the degree to which this disruption influences the stress field on an adherent cell. For this reason, the calculations performed in this study will provide a description of the stress field surrounding the cell (which could affect cell deformation), and the torque and force on the cell that must be balanced by receptor-ligand binding for a cell to adhere. The methods described in this paper are applied to rigid models of cells, but are extendable to the analysis of deformable cells. The present study could thus be considered a baseline for determining the importance of cell deformation for cell adhesion behavior.

Received for publication 30 December 1997 and in final form 13 May 1998.

Address reprint requests to Dr. Donald Gaver, Department of Biomedical Engineering, Tulane University, New Orleans, LA 70118. Tel.: 504-865-5150; Fax: 504-862-8779; E-mail: donald.gaver@tulane.edu.

0006-3495/98/08/721/13 $2.00

Biofilm formation

A situation that is similar to leukocyte adhesion is biofilm formation. "Biofilm" is a general term describing the immobilization of cells on a substratum. An excellent review of biofilms and their importance is provided by Characklis and Marshall (1990). Biofilms are ubiquitous in nature, and can be either detrimental or beneficial. For example, biofilms can occur on teeth and gums, intestines, and within the urinary tract, where they pose health risks. In contrast, biofilms may be beneficial in the natural environment, where they are responsible for natural cleansing of groundwater. In situ bioremediation efforts depend upon the creation of microbial colonies within porous media, wherein the bacteria and pore dimensions are equivalent.

The development or improvement of effective strategies for in-situ bioremediation should be based upon a sound understanding of the detailed pore-level behavior of microorganisms within porous media. Bioavailability of microorganisms depends upon the local physicochemical conditions (e.g., pH, temperature, concentrations of dissolved gases and solutes) because they influence chemotaxis and flocculation, the propensity of microbes to aggregate and adhere to each other and the local pore structure, creating the biofilm. A common feature of many theoretical models of biofilm formation is that the explicit dependence upon fluid dynamics is ignored. However, cells may be removed from the biofilm by flow properties that lead to detachment. In addition, while the biofilm is the site of bioremediation, it may also hinder microbial migration into the pores by reducing forced convection and diffusive transport of new cells into the small pores (a type of biofouling). For these reasons, recent studies of bacterial movement in microchannels suggest that surface interaction and hydrodynamic forces must be included in models at the micropore scale if one is to examine cell fate and transport issues in realistic models of bioremediation (Berg and Turner, 1990; Dillon et al., 1995, 1996; Harkes et al., 1992). The goal of the research described in this paper is to explain simply the fluid dynamical interaction between adherent cells and the flow through the microchannels they inhabit, so as to improve the understanding of this aspect of the microscale process. Additionally, knowledge of the force and torque on individual cells will be important in assessing the likelihood of biofilm formation.

Mechanotransduction

Recently it has become evident that vascular endothelial cells that line vessel walls convert fluid stresses to electrical and/or biochemical signals, affecting the behavior of the vascular system—a behavior termed *mechanotransduction* (Davies, 1995). This mechanism is hypothesized to regulate vessel tone and may be related to atherosclerosis. Tensegrity architectural models of the cytoskeleton may explain how the surface mechanical stresses are converted into biochemical responses (Ingber, 1997). A critical aspect of mechanotransduction studies is a quantitative evaluation of the stress field exerted on the cell surface. This aspect has been recognized and studied by Barbee and colleagues (Barbee et al., 1995), who used computational fluid dynamics tools to investigate how endothelial cell remodeling influences the subcellular shear stress distribution. These studies showed that the endothelial surface would remodel under shear so as to align with the flow to reduce the magnitudes of shear-stress and their gradients at the cell surface. Further understanding of the fluid mechanical interactions with adherent cells in a variety of orientations may be useful for identifying mechanotransduction mechanisms. While the problem described in the present paper is idealized, the methods described may be useful in further research of mechanotransduction. In particular, the change in the stress field with cell deformation (on which the present study builds a foundation) may be important in understanding mechanotransduction mechanisms.

Study goals

In the present study, our goal is to estimate the magnitudes of fluid-induced stress, force, and torque on a cell that adheres to a microchannel wall. As explained above, this information is essential if one is to accurately evaluate the adhesion strength necessary for a cell to remain adherent to either a vessel wall or on a soil matrix in porous media. In addition, to quantify mechanotransduction responses, one must first understand the magnitude and distribution of stresses on the cell membrane. We investigate a two-dimensional model of a single isolated cell within a narrow channel, and study the influence of channel height and cell size on the stresses, forces, and torques exerted on these cells. We use lubrication theory as a motivation for the development of simple algebraic formulae that can be used accurately to predict these mechanical influences over a range of different cell to channel height aspect ratios. Although the problem studied herein is greatly simplified, the methods described may be useful in determining improved analytical expressions for more complex systems that more accurately describe cell behavior in vivo.

In these models, we assume the flow is driven by a pressure difference (ΔP) between opposite ends of the channel of length L, thus setting the average pressure gradient. For this reason, the flow rate (Q^*) through the channel will depend upon the size of the channel as well as the size of the adherent cell. We have chosen to model this system as pressure-driven (instead of with a defined flow rate), because in the systems that we hope to model (e.g., porous media or capillary beds), parallel pathways may exist through which flow will be shunted when the resistance of a given pathway increases. In these cases, the pressure difference will remain relatively constant as cell adhesion occurs. In our simulations, we will report the flow rate that occurs with cell adhesion, because this will influence the base level of the stresses in the system, and the rate at which cells might convect into the channel.

MODEL DEVELOPMENT

Here we develop a model that can be used to study the stress distribution on individual cells in a single microchannel of length L and height H. These cells could be leukocytes adhering to the endothelial surface of a vessel wall, or could make up a biofilm in porous media. Flow of a viscous, incompressible fluid is driven within the channel because of an applied pressure difference ΔP. Discrete cells of height R are allowed to attach to the channel wall, which changes the "effective" wall shape and therefore influences the flow field. Below we develop the governing equations that describe this situation, and use this model to investigate the flow through the channel, and the fluid-mediated stresses on attached cells.

Governing equations

We assume slow, viscous flow through the microchannel in which inertia is negligible, based upon the Reynolds number, $Re = UH/\nu \ll 1$, where U is a representative flow velocity and ν is the fluid kinematic viscosity. Therefore, flow is governed by Stokes equations and continuity:

$$\nabla^* p^* = \mu \nabla^{*2} \mathbf{u}^*, \quad \text{and}$$
$$\nabla^* \cdot \mathbf{u}^* = 0. \tag{1}$$

where $\nabla^* p^*$ is the pressure gradient, μ is the viscosity of the fluid, and $\mathbf{u}^* = (u^*, v^*)$ is the convective velocity of the fluid. In this and following equations, * denotes a dimensional variable, and unstarred quantities reflect dimensionless variables.

Because of the imposed pressure difference, ΔP, the pressure on the left and right boundaries of the domain, P_{left} and P_{right}, are given by

$$p^*_{\text{left}} = \Delta P \quad \text{and} \quad p^*_{\text{right}} = 0, \tag{2}$$

where the pressure at the right boundary is taken as the reference pressure. The no-slip boundary condition is imposed so that the velocity at the top and bottom walls of the pore is zero:

$$\mathbf{u}^*(x^*, y^* = y^*_{\text{wall}}) = 0. \tag{3}$$

A monolayer biofilm develops when cells attach to the wall and modify the microchannel structure. At the point of attachment for each cell, the wall of the microchannel is modified by the addition of a semicircular protuberance of height R. The attachment is smoothed at the juncture with the wall by a "fillet" of radius $R/10$.

Scales and dimensionless governing equations

To discern important parameters of the system, the governing equations of the model are nondimensionalized by using the following scales:

$$x^* = Lx, \quad y^* = Ly, \quad p^* = \Delta P p, \quad \boldsymbol{\tau}^* = \Delta P \boldsymbol{\tau}$$
$$\text{and} \quad u^* = Uu = \frac{\Delta P H^2}{8\mu L} u, \tag{4}$$

where L and H are the length and height of the pore respectively, ΔP is the applied pressure difference across the length of the pore, and μ is the viscosity of the fluid. The velocity scale, $U = \Delta P H^2/8\mu L$, is the centerline velocity magnitude for flow in a channel without aggregation.

Using the scales in Eq. 4, the Stokes equations and continuity are given by

$$\nabla p = \frac{\beta^2}{8} \nabla^2 \mathbf{u}, \quad \text{and}$$
$$\nabla \cdot \mathbf{u} = 0. \tag{5}$$

The pressure and velocity boundary conditions are given by

$$p_{\text{left}} = 1 \quad \text{and} \quad p_{\text{right}} = 0, \tag{6}$$

and

$$\mathbf{u}(x, y = y_{\text{wall}}) = 0, \tag{7}$$

where $\beta = H/L$ is the dimensionless parameter defining the microchannel aspect ratio. In dimensionless form, cell adhesion induces a wall protuberance of magnitude $\alpha = R/L = \beta\gamma$, where $\gamma = R/H$ is the cell to channel width aspect ratio. An example of the domain with a single cell attached at $x = (1/2, 0)$ is shown in Fig. 1. We solve the governing equations using the boundary element method, as discussed in the Appendix. This computational method is outstanding for irregularly shaped domains, because it demands only a discretization of the surface. Even so, this method is capable of resolving fine features of the flow. For example, streamlines are shown in Fig. 1, which demonstrate the overall flow field. These streamlines show small Moffat vorticies near the edge of the cell, which would require small discretizations to resolve if finite difference methods were used. The boundary element method is useful for systems with free surfaces (e.g., deformable cells) (Gaver et al., 1996), because it does not require remeshing of the domain with deformation. Finally, this method is rapid—typical

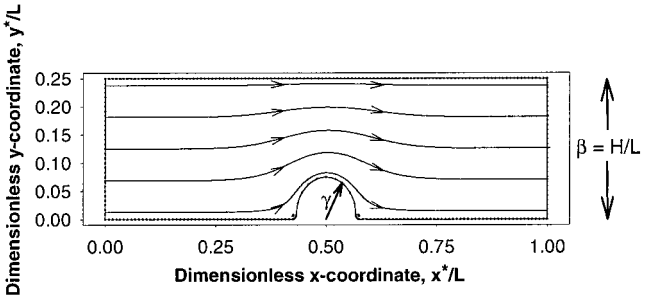

FIGURE 1 Example of a domain with one aggregated cell with streamlines indicating the flow. $\gamma = R/H = 0.30$; $\beta = H/L = 0.25$.

calculations required only 1 CPU-s on a 200 MHz Intel Pentium-Pro computer. For these reasons, the present methods are extendable to much more complicated systems that include multiple cells and/or cell deformation, from which the present study would be considered a baseline.

It is important to recognize that the scaling in this analysis removes the pressure difference between ends of the pore (ΔP) as a parameter of the problem, because it was used in the stress and velocity scales. To determine the magnitude of ΔP under specific conditions, one would use either direct measurements in an experiment, or estimate the magnitude based upon flow conditions that are known to exist. For example, if a background flow in a pore of dimensions $H = 10$ μm and $L = 100$ μm is known to be $U = 15$ μm/s (1.3 m/day, a natural flow velocity), then from Eq. 4 a pressure drop of $\Delta P = 1.2$ N/m^2 must be imposed across the pore. A reduction of H to 1 μm would yield a 100-fold increase in ΔP for the same velocity, or a 100-fold decrease in velocity for the same ΔP. We will demonstrate below that the stress/flow is invariant with ΔP, so a measurement of Q^* is sufficient to estimate the stresses on individual cells.

RESULTS

In this section we explore how the flow over attached cells establishes a stress field upon the cell. We first examine (next section) the flow rate through the system, Q^*, and demonstrate its behavior as a function of the two dimensionless parameters in the system, $\beta = H/L$ and $\gamma = R/L$. We then examine the scales for the magnitudes of the stresses, forces, and torques and show that these mechanical quantities are proportional to Q^*, and that the magnitudes of the flow-normalized quantities are independent of ΔP. Next, we predict the magnitudes of these flow-normalized mechanical properties on isolated cells and develop regression formulae based upon lubrication analysis. These regression formulae may be used simply to predict the fluid flow behavior on cells in constrained settings.

The influence of cell adhesion on channel flow rate

When a cell attaches to the channel wall, it disturbs the flow rate through the channel, $Q^* = \int u^* \mathrm{d}y^*$, which in turn influences the stress field experienced by the cell. We scale Q^* by the flow rate that would exist in a flat-walled (cell-free) system,

$$Q_{\text{flat-wall}} = \frac{\Delta P H^3}{12 \mu L}, \tag{8}$$

and define this dimensionless flow rate as

$$\tilde{Q} = \frac{Q^*}{Q_{\text{flat-wall}}} = \frac{12 \mu L \int u^* \mathrm{d}y^*}{\Delta P H^3}. \tag{9}$$

Deviation of $\tilde{Q}$ from unity represents the reduction in flow rate due to the cell adhesion. $\tilde{Q}$ depends on the two geometric dimensionless parameters in the system. The cell aspect ratio ($\gamma = R/H$) dictates the size of the gap width between the channel wall and top of the cell. Clearly, as $\gamma \rightarrow 1$, the channel becomes obstructed and $\tilde{Q} \rightarrow 0$. In addition, $\tilde{Q}$ is modulated by the other independent parameter of the system (either $\beta = H/L$ or $\alpha = R/L$). If $\gamma = R/H$ is varied with $\beta = H/L$ fixed, this is equivalent to changing the cell size (R) for a given channel, as shown in Fig. 2 *a*. In this case, as R/H increases, the cell fills a larger portion of the channel by increasing its relative length, because $R/L = R/H \cdot H/L$. The influence of flow following this scenario is presented in Fig. 3 *a*. This flow rate reduction occurs for two reasons. First, the resistance increases with increasing R/H due to the decreased gap through which fluid can flow between the cell and opposing wall. Second, the flow resistance increases because of the increasing axial extent over which the cell fills the channel (R/L increasing). Alternatively, varying R/H with R/L fixed is identical to changing the channel height (H) with a fixed cell size, as shown in Fig. 2 *b*. The influence on the flow rate in this situation is given by Fig. 3 *b*. In this case, the change in flow resistance is due only to the decrease in the gap width between the top of the cell and the opposite wall with increasing R/H. From this figure it is evident that small cells ($R/L = 0.01$) have only a minor effect on the flow rate until $R/H > 0.3$. However, as R/L increases, the flow resistance increases markedly because of the increasing axial extent of the flow disturbance.

Stress, force, and torque scales for attached cells

A number of mechanical factors may influence a cell's ability to adhere to a microchannel wall. These include the normal and shear-stress distribution on the cell membrane, and the net force and torque exerted on the cell. Below we determine the basic magnitudes of these characteristics, so that we can determine the relative influence of fluid flow on a cell. As described in detail below, we rescale the cell shear stress (τ_s^*), the x component of force (F_x^*), and the torque (T^*) by magnitudes that are derived from stress magnitudes

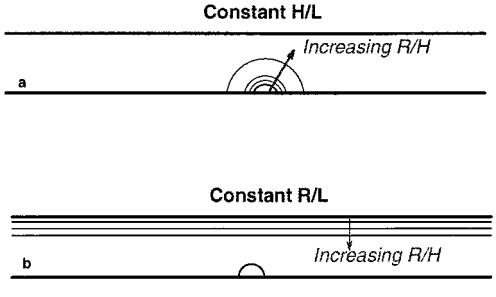

FIGURE 2 Description of decrease in the cell aspect ratio, R/H, by (*a*) changing the cell size ($\beta = H/L$ fixed); (*b*) changing the channel width ($\gamma = R/L$ fixed).

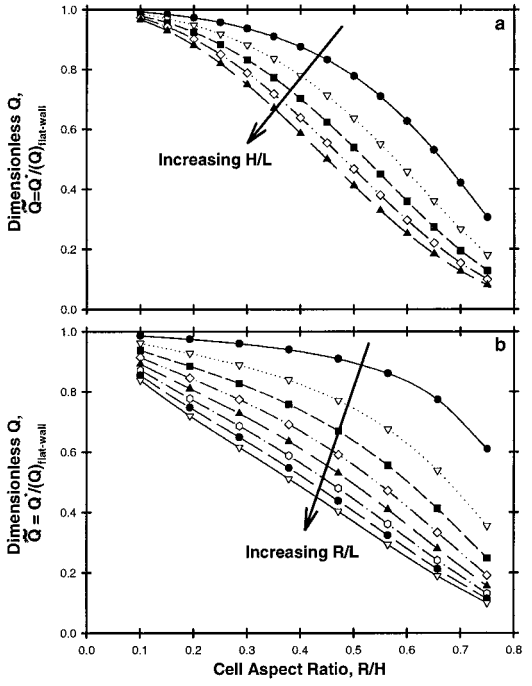

FIGURE 3 The influence of cell aspect ratio (R/H) on the flow rate through the channel. (*a*) Effect of variation in cell size (H/L fixed). ·, H/L = 0.05; ∇, H/L = 0.10; ■, H/L = 0.15; ◊, H/L = 0.20; ▲, H/L = 0.25. (*b*) Effect of variation of channel height (R/L fixed). —·—, R/L = 0.01; ····∇····, R/L = 0.03; —■—, R/L = 0.05; —◊····, R/L = 0.07; —▲—, R/L = 0.09; —· ····, R/L = 0.11; —●····, R/L = 0.13; —∇—, R/L = 0.15.

that would exist in a flat-wall (or cell-free) system. These rescaled dimensionless quantities are denoted by $\tilde{\tau}_s$, $\tilde{F}_x$, and $\tilde{T}$, respectively. These quantities provide a measure of the amplification of the fluid mechanical interaction with the cell due to the combined effect of flow disruption by the cell and the constraint of the channel.

In addition, because shear stress under Stokes flow is directly proportional to Q^*, it is useful to represent the fluid mechanical interaction with the cells by dividing the stress, force, or torque by Q^*—we call this the *flow-normalized* response. This representation is beneficial for several reasons. First, it identifies the magnification of the mechanical influence on cells in a system with a fixed flow rate. In a pressure-driven system the flow rate is modified, as shown in Fig. 3. Nevertheless, with this representation, once Q^* is determined, it is simple to calculate the fluid mechanical impact on the cell. Most importantly, the flow-normalized responses (τ_s^*/Q^*, F_x^*/Q^*, and T^*/Q^*) depend only on physical constants of the system and the dimensionless flow-normalized responses ($\tilde{\tau}_s/\tilde{Q}$, $\tilde{F}_x/\tilde{Q}$, and $\tilde{T}/\tilde{Q}$, respectively) that are functions only of $\gamma = R/H$. This greatly simplifies the data representation, and will be very useful in determining regression formulae of the system response outlined below (see Regression Relationships).

To determine the magnitudes of these mechanical properties, the stress vector along the cell surface, $\boldsymbol{\tau}_{cell}$, is calculated using the relationship:

$$\boldsymbol{\tau}_{cell} = \frac{\boldsymbol{\tau}^*_{cell}}{\Delta P} = \boldsymbol{\sigma} \cdot \hat{\mathbf{n}}_{cell} \tag{10}$$

where $\hat{\mathbf{n}}_{cell}$ is the cell wall outward normal vector, and $\boldsymbol{\sigma}$ is the dimensionless stress tensor, $\boldsymbol{\sigma} = -P\mathbf{I} + (\beta^2/8)[\nabla\mathbf{u} + \nabla\mathbf{u}^t]$. An example of the x, y, normal, and tangential components of the stress (τ_x, τ_y, τ_n, and τ_s, respectively) on a single cell is shown in Fig. 4, *a–d*. Note that $\tau_y = \tau_n$ along the flat wall. Far from the cell, these quantities approach the pressure p, which decreases linearly, as would be expected in uniform channel flow.

Note that the dimensionless shear-stress on a flat-walled (cell-free) microchannel is

$$(\tau_s)_{flat\text{-}wall} = \frac{(\tau_s^*)_{flat\text{-}wall}}{\Delta P} = \frac{\beta}{2}, \tag{11}$$

which is shown in Fig. 4 *d*. This figure shows that τ_s on the cell surface may be much larger than that on the flat wall. To compare the relative magnitudes of the cell shear-stress with that exerted on the flat wall in a cell-free system, we represent the dimensionless shear-stress as

$$\tilde{\tau}_s = \frac{\tau_s^*}{(\tau_s^*)_{flat\text{-}wall}} = \frac{\tau_s^*}{\Delta P(\beta/2)}, \tag{12}$$

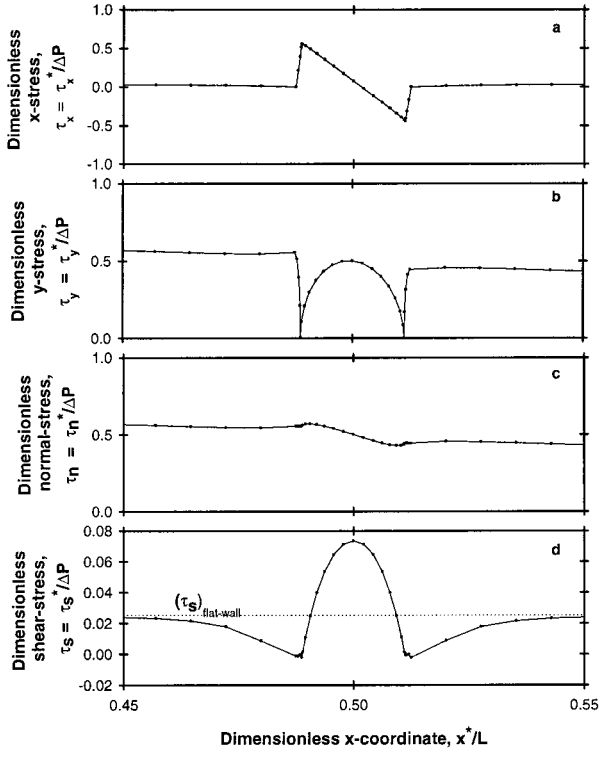

FIGURE 4 Dimensionless stresses exerted on single cells. $\beta = H/L$ = 0.05, $\gamma = R/H$ = 0.25. (*a*) x component; (*b*) y component; (*c*) normal component; (*d*) tangential component.

and the flow-normalized shear stress from Eq. 8 is thus

$$\frac{\tau^*_s}{Q^*} = \left(\frac{6\mu}{H^2}\right)\frac{\tilde{\tau}_s}{\tilde{Q}}. \tag{13}$$

The x component of the force/width on the cell (F^*_x) is computed by integrating τ^*_x over the cell surface. In undisturbed flow, the magnitude of force on a flat section of wall over the distance covered by the cell is

$$(F_x)_{\text{flat-wall}} = 2R(\tau^*_x)_{\text{flat-wall}} = R\beta\Delta P. \tag{14}$$

This magnitude is due solely to the shear-stress exerted on the flat wall. When a cell is introduced, τ^*_x will include contributions due to shear- and normal stresses, which will be modified by the flow field, increasing the magnitude of F^*_x. To identify the amplification due to flow disruption, we represent the relative magnitude of F^*_x with the flat-wall limit as

$$\tilde{F}_x = \frac{F^*_x}{(F_x)_{\text{flat-wall}}} = \frac{\int \tau^*_x ds^*}{R\cdot\Delta P\beta}, \tag{15}$$

where the integration is computed over the cell surface. The flow-normalized x component of force/width is thus

$$\frac{F^*_x}{Q^*} = \left(\frac{12\mu R}{H^2}\right)\frac{\tilde{F}_x}{\tilde{Q}} = \left(\frac{12\gamma\mu}{H}\right)\frac{\tilde{F}_x}{\tilde{Q}}. \tag{16}$$

The torque/width experienced by the cell is $\mathbf{T}^* = \int \mathbf{r}^* \times \boldsymbol{\tau}^* ds^*$, where $\mathbf{r}^*$ is typically the vector between the rotational axis of the cell and the cell surface. For unattached cells, $\mathbf{r}^*$ originates from the center of mass (denoted with the subscript cm) of the cell, so that $\mathbf{T}^*_{cm} = \int \mathbf{r}^*_{cm} \times \boldsymbol{\tau}^* ds^*$, with the integration conducted over the entire surface of the cell. In the present model, we assume that the cell is immobile. In this context, it is most convenient to choose $\mathbf{r}^* = \mathbf{r}^*_{base}$, the radial vector from the center of the attachment of the cell to the surface. In this case, the torque induced by fluid flow is $\mathbf{T}^*_{base} = \int \mathbf{r}^*_{base} \times \boldsymbol{\tau}^* ds^* = R\int \tau^*_s ds^*$, because the component of $\boldsymbol{\tau}^*$ perpendicular to $\mathbf{r}^*_{base}$ is τ^*_s. $\mathbf{T}^*_{base}$ is useful for representing the fluid-exerted torque on the fully adherent cell. In equilibrium it is balanced by the torque exerted by cell adhesion, which is due solely to the y component of force exerted by the receptor-ligand binding along the flat surface of the cell, whereas the x component of force exerted by the receptor-ligand binding is balanced by $\mathbf{F}^*_x$. For this reason, all torques hereafter will be referred to as $\mathbf{T}^*_{base}$ unless otherwise noted. Note, however, that because $\mathbf{r}^*_{cm} = \mathbf{r}^*_{base} - (4R)/(3\pi)e_y$, $\mathbf{T}^*_{cm} = \mathbf{T}^*_{base} + (4R/3\pi)\int \tau^*_x ds^* = \mathbf{T}^*_{base} + (4R/3\pi)F^*_x$. So, from the data provided, $\mathbf{T}^*_{cm}$ can be determined.

To determine a scale for $\mathbf{T}^*_{base}$, we assume that $\tau^*_s \approx (\tau^*_s)_{\text{flat-wall}}$ (which underestimates the stress in the cell center, but overestimates it near the edge of the cell); then a "flat-wall" torque/width scale is

$$(T^*_{base})_{\text{flat-wall}} = \pi R^2\left(\frac{\beta\Delta P}{2}\right). \tag{17}$$

Below, we will use this as a torque scale to evaluate the influence of biofilm formation on the torque experienced by a cell. As such, we will represent the dimensionless torque as

$$\tilde{T}_{base} = \frac{2R\int \tau^*_s ds^*}{(\pi R^2)(\beta\Delta P)}, \tag{18}$$

where the integration is taken over the cell surface. The flow-normalized torque is given by

$$\frac{T^*_{base}}{Q^*} = \left(\frac{6\pi\mu R^2}{H^2}\right)\frac{\tilde{T}_{base}}{\tilde{Q}} = 6\pi\mu\gamma^2\frac{\tilde{T}_{base}}{\tilde{Q}}. \tag{19}$$

Stresses, forces, and torques on individual cells

Fig. 5, *a* and *b*, shows the dimensionless shear-stress and normal stress for individual cells of different sizes within a narrow channel ($\beta = H/L = 0.05$). Fig. 5 *a* shows that small cells ($\gamma = R/H = 0.1$) have a $(\tilde{\tau}_s)_{max} \approx 3$, indicating that the shear-stress on a cell is much larger than the stress exerted on the flat wall. This result is in agreement with calculations of stresses due to Stokes flow in a semiinfinite domain over semicircular ridges computed by Higdon (1985), providing confirmation of our numerical method. This result shows that the shear-stress exerted on the cell is much larger than the stress exerted on the surrounding wall. The shear-stress deviation occurs over a distance from the cell center of several cell radii ($\sim 4R$) before $\tilde{\tau}_s \to 1$, indicating the distance over which the flow field is disturbed by the

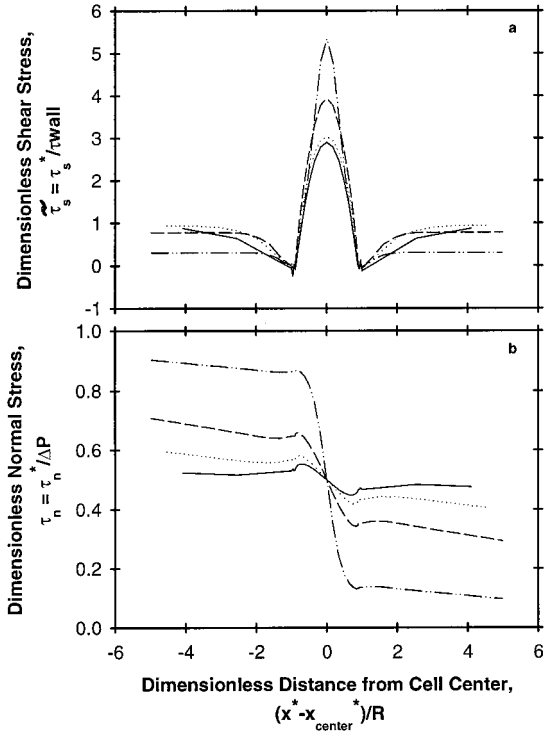

FIGURE 5 The relationship between cell aspect ratio (R/H) and cell stress. $\beta = H/L = 0.05$. ——, $R/H = 0.1$; ·····, $R/H = 0.3$; —, $R/H = 0.5$; ——···, $R/H = 0.75$. (*a*) Shear-stress; (*b*) Normal stress.

presence of the cell. With increasing cell size, $(\tilde{\tau}_s)_{max}$ increases, so that when $R/H = 0.75$, $(\tilde{\tau}_s)_{max} \approx 5.5$. The cell disturbs the flow field throughout the channel by introducing a large increase in flow resistance, which decreases $\tilde{Q}$ and causes the far-field $\tilde{\tau}_s < 1$. The relative disturbance from the far-field flow occurs over a shorter relative distance from the cell center of $\sim 2R$ with the larger cells.

The normal stress along the bottom wall is greatly influenced by R/H, as shown in Fig. 5 *b*. In a cell-free system, the normal stress is identically the pressure (p) and would decay linearly with increasing x; this is clearly modified by the introduction of a cell. The normal stress disruption causes an increase in P upstream of the cell, and a decrease downstream. This is a direct result of the increased flow resistance resulting from the cell occluding the channel.

Figs. 6–8 demonstrate the behavior of the system through plots of $(\tilde{\tau}_s)_{max}$, $\tilde{F}_x$, and $\tilde{T}_{base}$, respectively, for $\alpha = R/L = 0.03$ (a cell occupying a small section of the channel) and $\alpha = 0.10$ in the *a* panels, and the dimensionless flow-normalized mechanical behavior of the system, $(\tilde{\tau}_s)_{max}/\tilde{Q}$, $\tilde{F}_x/\tilde{Q}$, and $\tilde{T}_{base}/\tilde{Q}$, in the *b* panels. The *a*-panel representations are intended to give a general understanding of the physical behavior of the system. However, to completely analyze this system using this representation would require an exhaustive exploration as a function of two geometrical parameters (γ and either α or β). In contrast, using the flow-normalized (*b*-panel) approach, the response is solely

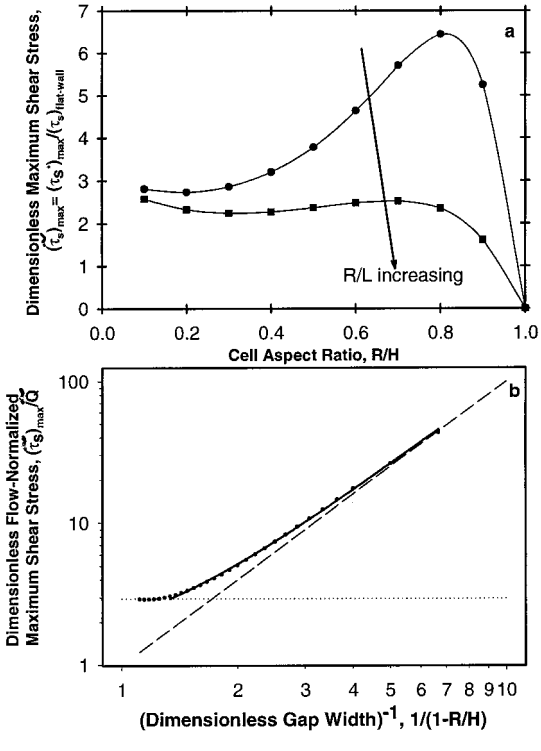

FIGURE 6 The influence of cell aspect ratio (R/H) on the maximum shear-stress. (*a*) Dimensionless behavior. ●, $\alpha = 0.03$; ■, $\alpha = 0.10$. (*b*) Dimensionless flow-normalized response. ●, Boundary element; – – –, lubrication theory; ·····, large-gap limit; ——, regression.

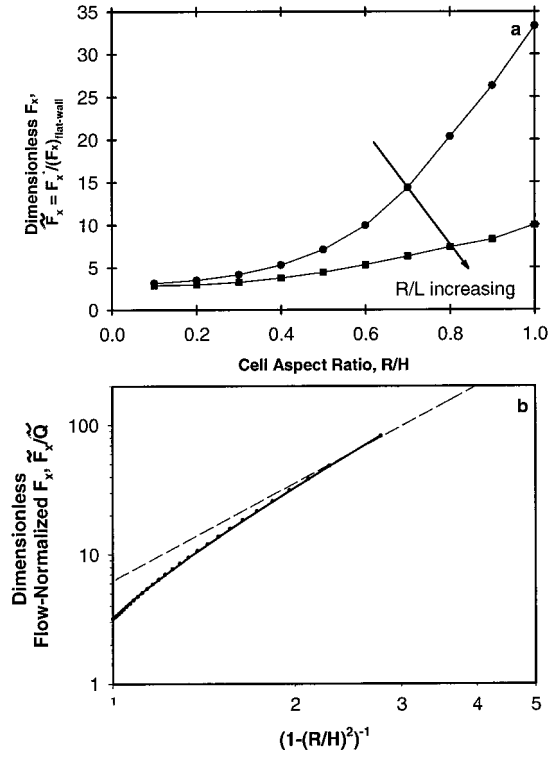

FIGURE 7 The influence of cell aspect ratio (R/H) on the x component of force, F_x. (*a*) Dimensionless response. ●, $\alpha = 0.03$; ■, $\alpha = 0.10$. (*b*) Dimensionless flow-normalized response. ●, Boundary element; – – –, lubrication theory; ——, regression.

a function of the dimensionless cell size, $\gamma = R/H$. These data are represented in log-log format, with variation of γ along the abscissa representing the inverse of the dimensionless gap width $1/(1 - \gamma)$ or by $1/(1 - \gamma^2)$. The rationale for this format will be made clear when data regression formulae are discussed in the next section.

Fig. 6 *a* shows the maximum $\tilde{\tau}_s$ exerted on the cell as R/H increases. For small R/H, $(\tilde{\tau}_s)_{max} \approx 3$, the infinite-domain limiting result discussed above. As R/H increases, $(\tilde{\tau}_s)_{max}$ increases greatly, and reaches a maximum near $R/H = 0.8$. For $R/H > 0.8$, $(\tilde{\tau}_s)_{max} \to 0$, because the cell obstructs the channel and $\tilde{Q} \to 0$. Cells that extend over a larger portion of the domain ($\alpha = 0.10$) experience smaller $(\tilde{\tau}_s)_{max}$ because of the commensurate reduction in flow rate in the pressure-driven system. Fig. 6 *b* demonstrates the influence of γ on the dimensionless flow-normalized maximum shear stress, $(\tilde{\tau}_s)_{max}/\tilde{Q}$. As the gap width decreases ($(1 - \gamma)^{-1}$ increasing), $(\tilde{\tau}_s)_{max}/\tilde{Q}$ is initially constant, indicating that the top wall has little influence on the cell. When $(1 - \gamma)^{-1} > 1.33$, shear stress amplification due to interaction with the top wall is observed. This indicates that the top wall starts to influence the shear stress on the cell when the cell size is greater than 25% of the channel width. For larger cells, a dramatic increase in $(\tilde{\tau}_s)_{max}/\tilde{Q}$ occurs as the cell fills the channel. In a system with a fixed flow rate, $(\tilde{\tau}_s)_{max}$ would increase exponentially; however, in a pressure-driven system, the shear-stress would be reduced from these values by the reduction in $\tilde{Q}$ (see Fig. 3), as shown in Fig. 6 *a*.

The dimensionless x component of force on a cell, $\tilde{F}_x$, as a function of $\gamma = R/H$ is given in Fig. 7 *a*. For R/H small, $\tilde{F}_x \approx 3$, indicating the magnification of force due to flow disruption, even for very small cells. As γ increases, $\tilde{F}_x$ increases markedly. In the limit $R/H \rightarrow 1$, the cell completely occludes the channel, and thus $\tilde{F}_x \rightarrow L/R = 1/\alpha$ (in dimensional form, $F_x^* \rightarrow \Delta P \cdot H$), because this is the entire x component of force applied to the cell. The dimensionless flow-normalized x component of force on a cell ($\tilde{F}_x/\tilde{Q}$) as a function of $(1 - \gamma^2)^{-1}$ is shown in Fig. 7 *b*. This representation shows that in a fixed flow-rate system, $\tilde{F}_x$ would increase without bound because the applied pressure would need to be increased to compensate for the increased viscous resistance as the gap width between the cell and top wall narrows. In a pressure-driven system, the $\gamma \rightarrow 1$ limiting behavior is not as obvious in Fig. 7 *b*, because $\tilde{Q}$ is simultaneously reduced with the increase in γ, as shown in Fig. 3.

Finally, the dimensionless torque $\tilde{T}_{base}$ is greatly influenced by R/H, as shown by Fig. 8. Fig. 8 *a* shows that as γ increases, the torque experienced by the cell increases to a maximum value, then decays to zero as the flow is reduced by obstruction of the channel. The dimensionless flow-normalized response shown in Fig. 8 *b* demonstrates that in the flow-driven case, $\tilde{T}_{base}$ would grow exponentially as γ increases. This increase in $\tilde{T}_{base}$ is reduced by flow limitation in the pressure-driven system, as demonstrated in Fig. 8 *a*. These results show that torque predictions in unconstrained systems may greatly underestimate the torque on a cell in a constrained channel.

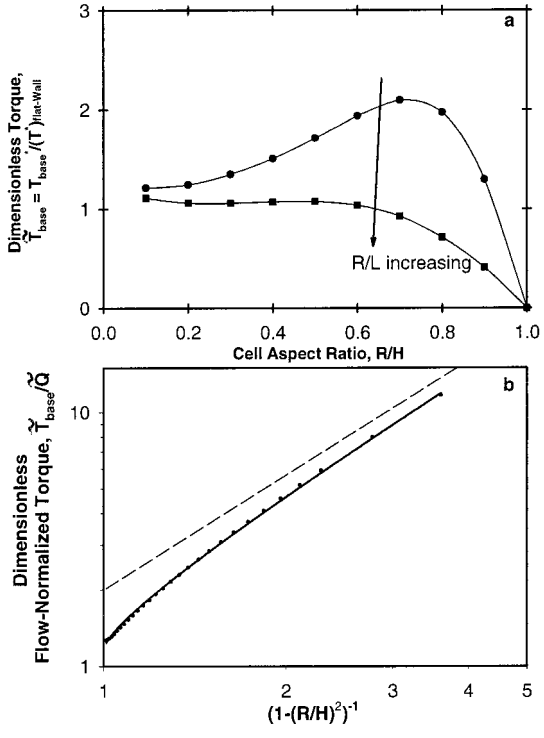

FIGURE 8 The influence of cell aspect ratio (R/H) on the cell torque. (*a*) Dimensionless response. ●, $\alpha = 0.03$; ■, $\alpha = 0.10$. (*b*) Dimensionless flow-normalized response. ●, Boundary element; – – –, lubrication theory; ——, regression.

Regression relationships

The data presented in Figs. 6–8 clearly demonstrate that disruption of the flow field by a single cell in a microchannel can greatly increase the mechanical influence of the fluid on the cell over that experienced in an unconstrained setting. In this section we develop regression relationships that can be used to predict simply these fluid mechanical interactions for individual cells. For the flow-normalized responses, the general forms of these regressions were derived using lubrication theory analysis, which is presented briefly in the Appendix. This approach gives a logical basis for the regression analysis. The general forms derived should thus be accurate for more complex systems (deformable and multicell), which will allow comparison with the rigid single-cell responses derived herein.

Flow rate

The flow rate predictions by lubrication theory given in the Appendix for a semicircular protuberance of length $\alpha = R/L$ and channel aspect ratio $\beta = H/L$ gives

$$\tilde{Q} = \frac{Q}{Q_{flat\text{-}wall}} = \frac{f_1(\alpha, \beta)}{f_2(\alpha, \beta)},$$

where

$$f_1(\alpha, \beta) = 2(\beta^2 - \alpha^2)^{5/2} \tag{20}$$

and

$$f_2(\alpha, \beta) = (2(1 - 2\alpha)\alpha^4 + 2\beta^2\alpha^2(5\alpha - 2))(\beta^2 - \alpha^2)^{1/2} + \beta^4(2(\beta^2 - \alpha^2)^{1/2} + 3\pi\alpha^2) + 6\beta^4\alpha^2\tan^{-1}\left(\frac{\alpha}{(\beta^2 - \alpha^2)^{1/2}}\right),$$

as demonstrated in Fig. 9. Although this approximation

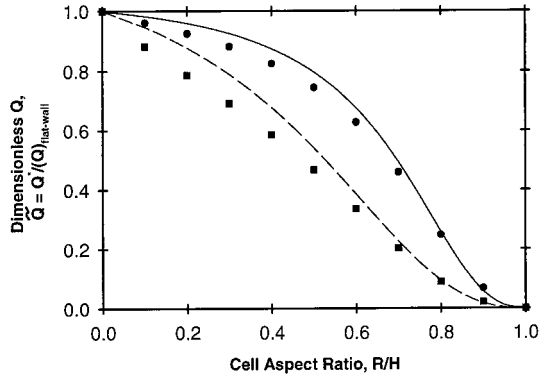

FIGURE 9 The influence of cell aspect ratio (R/H) on flow rate through the channel. Boundary element analysis: ●, $\alpha = 0.03$; ■, $\alpha = 0.10$. Lubrication theory: ——–, $\alpha = 0.03$; ——, $\alpha = 0.10$.

overestimates $\tilde{Q}$ for small R/H, it gives a better fit than any simple regression formula provides, and is probably sufficient for the purposes of this study.

Maximum shear stress

Lubrication theory shows that

$$\lim_{\gamma\to 1}\left(\frac{(\tilde{\tau}_s)_{max}}{\tilde{Q}}\right)=\frac{1}{(1-\gamma)^2}. \tag{21}$$

As shown in Fig. 6 *a*, this relationship is satisfactory for small gap widths, but does not provide an adequate relationship for small values of γ, as can be seen in Fig. 6 *b*. To develop a quantitative relationship that can be used over $0.25 \le \gamma \le 1$ (the range over which the top wall influences the cell), we performed a least-squares regression of the boundary element data, using the form $(\tilde{\tau}_s)_{max}/\tilde{Q} = a + 1/(1-\gamma)^2$, which has the correct limiting behavior as $\gamma \to 1$. This calculation shows that $a = 1.158$, and the regression coefficient is $R^2 = 0.998$. This leads to the following relationship for the maximum shear stress calculations:

$$\left(\frac{(\tilde{\tau}_s)_{max}}{\tilde{Q}}\right)=\begin{cases}2.95 & \gamma<0.25\\ 1.158+\dfrac{1}{(1-\gamma)^2} & 0.25\le\gamma\le 0.85.\end{cases} \tag{22}$$

This relationship is shown in Fig. 6 *b*, which demonstrates a strong correlation to the calculations from the boundary element method and to that of the limiting lubrication theory analysis. For $\gamma > 0.85$, Eq. 21 should be used to estimate $(\tilde{\tau}_s)_{max}/\tilde{Q}$.

x component of force, F_x:

As shown in the Appendix, the lubrication approximation for $(\tilde{F}_x/\tilde{Q})$ gives

$$\lim_{\gamma\to 1}\left(\frac{\tilde{F}_x}{\tilde{Q}}\right)=\frac{2\pi}{(1-\gamma^2)^{5/2}}, \tag{23}$$

which is shown in Fig. 7 *b*. Clearly this relationship is inadequate for $\gamma < 1$. We generalized this form and found the regression

$$\frac{\tilde{F}_x}{\tilde{Q}}=\frac{3.19+0.65\gamma+4.3\gamma^2}{(1-\gamma^2)^{5/2}} \qquad \gamma\le 0.8, \tag{24}$$

which, as shown in Fig. 7 *b*, clearly provides a good fit of the computationally derived results ($R^2 = 1.00$). For $\gamma > 0.8$, Eq. 23 should be used to estimate $\tilde{F}_x/\tilde{Q}$.

Torque

In the limit of small gap width, the flow-normalized torque on the cell is given by

$$\lim_{\gamma\to 1}\left(\frac{\tilde{T}_{base}}{\tilde{Q}}\right)=\frac{2}{(1-\gamma^2)^{5/2}}, \tag{25}$$

as shown in Fig. 8 *b*. We generalized this form and found the regression

$$\frac{\tilde{T}_{base}}{\tilde{Q}}=\frac{1.15+0.70\gamma}{(1-\gamma^2)^{5/2}} \qquad \gamma\le 0.85, \tag{26}$$

which (Fig. 8 *b*) clearly provides a good fit of the computationally derived results ($R^2 = 1.00$). Over the range of γ investigated, this relationship does not converge to the lubrication theory prediction given in Eq. 25, although as $\gamma \to 1$, it is expected that this relationship will hold.

DISCUSSION

In this paper we predict the stress, force, and torque on a model of a stationary cell attached to a channel wall. From the data presented above, it is clear that the flow-field disruption can be significant. The constraints added by the microchannel walls result in significant magnification of the stress, force, and torque when the cell size is significant in relation to the channel width. In this case, the amplification of the cell stress, force, and torque can be large, as demonstrated by Figs. 6–8. In a pressure-driven system, the net flow is reduced by this disturbance, as shown in Figs. 3 and 9, which reduces the stress amplification. If the cell is small compared to the channel length ($R/L \ll 1$), this flow rate reduction is lessened. In a system with a defined flow rate, the stress amplification is potentially enormous, because the flow is required to squeeze through the gap between the cell and the opposing wall. This case is described by panels *b* of Figs. 6–8. From these studies, it appears that the stress magnification demonstrated in this model may have a significant impact on cell adhesion within the channel, or on the mechanotransduction of cells lining the channel wall.

As with all model studies, it is important to keep in mind the limitations of the modeling approach. In particular, with this model we have assumed a two-dimensional geometry that implies that the cell shape does not vary in the z direction, and thus our cells are semicircular "rib-shaped" objects, instead of a more biological hemispherical shape. We have also neglected to model cell wall flexibility, which will clearly allow modification of the cell shape when large stresses are imposed. Furthermore, in the models we assumed that fluid inertia was negligible, based upon $Re = UH/\nu$. For a flow velocity appropriate for the microvasculature with $U = 0.2$ cm/s, $H = 20$ μm, and $\nu = 0.03$ cm^2/s, $Re = 0.01$; thus inertia is indeed negligible. If the gap width is reduced with Δp held constant, then the reduction in the flow rate (see Fig. 3) would further reduce Re. If Q is defined, then a reduction in the gap width would be accompanied by an increase in U, which would elevate Re. If the gap width reduces to 10% of the channel width ($\gamma = 0.9$), then $Re = 0.1$, which is large enough for inertial effects to

be significant. If this regime is to be investigated, modification of the analytical methods will be warranted.

Validation

To judge the accuracy of the two-dimensional modeling approach in the present study, we compared our predictions to calculations and measurements of three-dimensional flow obstructions in different flow scenarios by other investigators (Brooks and Tozeren, 1996; Chapman and Cokelet, 1996; Pozrikidis, 1997). To do so, it was necessary to calculate an equivalent 3-D force and torque on our 2-D objects. We chose to let $(F_x^*)_{3\text{-D}} = 2R(F_x^*)_{2\text{-D}}$, where $(F_x^*)_{2\text{-D}}$ is the prediction from the present study, and $(F_x^*)_{3\text{-D}}$ is the force on the cell in a cell of length $2R$, which should thus be comparable to a hemispherical cell. Likewise, $(T^*_{base})_{3\text{-D}} = 2R(T^*_{base})_{2\text{-D}}$.

Our first comparison is to the model study by Pozrikidis (1997) of shear flow over a protuberance attached to a plane wall, which can be compared to our study in the limit of $\gamma \rightarrow 0$. In this study, far upstream the imposed flow field has a linear velocity, so that $u = ky$, and thus $(\tau_s^*)_{\text{flat-wall}} = \mu k = \Delta p\beta/2$, which sets the flow rate in our system at $Q^* = kH^2/6$. From this, our model studies in the limit of $\gamma \rightarrow 0$, using Eqs. 16 and 24, predict $(F_x^*)_{3\text{-D}} = 4.06\pi\mu kR^2$. Likewise, Eqs. 19 and 26 give $(T^*_{base})_{3\text{-D}} = 2.30\pi\mu kR^3$. For comparison, Pozrikidis (1997) predicts $(F_x^*)_{3\text{-D}} = 4.30\pi\mu kR^2$ and $(T^*_{base})_{3\text{-D}} = 2.44\pi\mu kR^3$. This difference of only 6% is surprisingly good.

Next, we compare the results of our model to the study results of Brooks and Tozeren (1996), who modeled cells attached to a flow channel. These models explored arrays of a variety of different shaped cells, and we compare our model results to their prediction for an array of hemispherical cells of radius $R = 12.6$ μm in a channel of height $H = 120$ μm ($\gamma = 0.105$). In this model an intercell spacing of $d = 60$ μm exists and a flow rate $(Q^*)_{3\text{-D}} = 10$ ml/min occurs in a channel of width $b = 1.5$ cm, and the fluid viscosity is $\mu = 0.01$ dyn s/cm^2. Our model predicts $(F_x^*)_{3\text{-D}} = 9.9 \times 10^{-4}$ dyn, which is only a 6% deviation from their prediction of $(F_x^*)_{3\text{-D}} = 9.3 \times 10^{-4}$ dyn. It should be noted, however, that in this case, our model prediction is larger than the prediction by Brooks and Tozeren (1996), whereas we predict a smaller force than that predicted by Pozrikidis (1997). This discrepancy is due most likely to interactions between neighboring cells in the study of Brooks and Tozeren (1996), which reduces $(F_x^*)_{3\text{-D}}$, and was not modeled in either the present study or by Pozrikidis (1997). Once again, the prediction between the present 2-D study and the 3-D calculation is very good.

Finally, we consider F_x^* for a single cell, and compare it to experimental measurements and computational predictions by Chapman and Cokelet (1996, 1997) of the drag force on a model leukocyte adhering to a blood vessel. In these studies, the authors determined the drag force on a rigid sphere attached to the inside wall of a cylindrical tube with a prescribed flow rate through the tube. Using dimensional analysis, they find that

$$\left(\frac{F_x^*}{Q^*}\right)_{\text{tube}} = \frac{\gamma_{\text{tube}}{}^2\mu}{2D}\left(8.15 - \frac{7.52}{\ln(\gamma_{\text{tube}})}\right)^2, \qquad (27)$$

where $\gamma_{\text{tube}} = d/D$ is the ratio of the cell to tube diameter. Fig. 10 *a* compares the relative magnitudes of the dimensionless quantities $(F_x^*/Q^*)/(\mu\gamma/\mathcal{L})$ for the 2-D channel regression behavior (Eq. 24) with the 3-D tube measurements (Eq. 27), where $\mathcal{L}$ is the relevant cross-sectional dimension (H for 2-D, or D for 3-D). Note that F_x^*/Q^* is dimensionally equivalent in 2-D and 3-D, because in 2-D F_x^* is the force per unit width and Q^* is the flow per unit width, so the two-dimensionality of each cancels out. This figure shows a remarkable similarity between the 2-D channel predictions and 3-D measurements. Fig. 10 *b* shows that for $\gamma > 0.5$, the 2-D prediction consistently overestimates F_x^* by only 25%, indicating that for small gap widths the fluid dynamics are fit by 2-D approximations. This comparison suggests that stress and torque predictions of the 2-D channel model may give reasonably accurate results for small gap widths, because most of the contributions to the stress field occur in the narrow region between the cell and opposite wall, which has a 2-D behavior when the gap width is small. Of course, this hypothesis should be evaluated in a careful comparison between 2-D and 3-D calculations. Nevertheless, this comparison gives us confidence that the predicted amplification of cell stress, torque, and force exerted in small channels is relevant to the 3-D system.

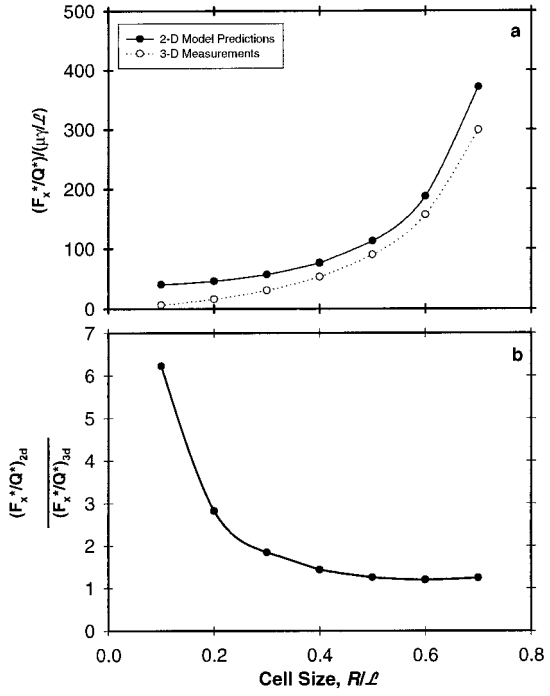

FIGURE 10 Comparison of F_x predictions with 3-D experiments in tube. (*a*) $F_x^*/Q/(\mu\gamma/\mathcal{L})$. (*b*) Proportional difference in predictions.

As an example of how the analysis above may be used to predict the fluid mechanical influence on adherent cells, we consider neutrophil adhesion in a postcapillary venule. The relevant dimensions are $d = 8$ μm for the neutrophil, $D = 20$ μm for a postcapillary venule (Horsfield and Gordon, 1981), $L = 1000$ μm, $\mu = 0.03$g/(cm s), with an average fluid velocity of $V_m = 0.2$ cm/s, resulting in a 3-D flow rate $Q_{3\text{-D}}^* = 6.3 \times 10^{-7}$ cm^3/s. We will assume in this system that $d \approx R$ and $D \approx H$, which is justified based upon the comparison between tube experiments and channel theory above. From Eqs. 24 and 26, $\tilde{F}_x/\tilde{Q} = 6.4$ and $\tilde{T}_{base}/\tilde{Q} = 3.1$, respectively. So from Eq. 16, $F_x^* = 2.9 \times 10^{-4}$ dynes. And from Eq. 19, $T_{base}^* = 1.8 \times 10^{-7}$ dynes · cm. For the neutrophil to stop rolling, the ligand-receptor binding would need to create a torque of this magnitude. From Eq. 26, this is nearly three times the torque one would predict in an unconstrained setting. To calculate the shear-stress on the cell, an equivalent 2-D flow rate must be calculated for this system. We choose $Q_{2\text{-D}}^* = 32Q_{3\text{-D}}^*/(6\pi D) = (4/3)V_m D$, so that τ_s^* from Eq. 13 correctly predicts the vessel wall shear-stress in a cell-free system. So in this case, $Q_{2\text{-D}}^* = 5.3 \times 10^{-4}$ cm^2/s. Then from Eqs. 13 and 22, $\tau_s^* \approx 100$ dynes/cm^2. These predictions are clearly subject to error due to differences in 2-D and 3-D geometry. However, in all cases these results are comparable to predictions made by Fung (1984), based upon the model studies by Schmid-Schoenbein et al. (1975). Finally, from Fig. 9, the flow rate through this venule would not be greatly affected by the adhesion of the cell, because $\alpha = R/L \ll 1$. However, if L is reduced to 350 μm, the flow (and hence F_x^*, T_{base}^*, and τ_s^*) would be reduced by ~20%. This could have an impact on the rate of leukocyte transport to this venule by shunting blood to other parallel venules.

CONCLUSIONS

In this study, we have attempted to clarify the importance of fluid mechanics for the stresses, forces, and torques experienced by cells adhering to microchannel walls. This situation is important in biofilm formation, and cell adhesion in biomedical systems. We have shown that the stress magnification due to cells adhering in a constrained setting may be extremely large, which may have an impact on the likelihood of adhesion, the flow rate through the channel, and mechanotransduction. We have used the boundary element method to perform the calculations in this study, and have used lubrication theory to determine simple analytical expressions that can be used to predict the maximum shear stress, force, and torques on 2-D representations of immersed cells. We used these relationships to create formulae for 3-D immersed objects. These formulae are

$$(\tau_s^*)_{max} = \frac{6\mu Q_{2\text{-D}}^*}{H^2}\begin{cases} 2.95 & \gamma < 0.25 \\ 1.158 + (1-\gamma)^{-2} & 0.25 \le \gamma \le 0.85 \end{cases},$$

$$(F_x^*)_{3\text{-D}} = 24\mu\gamma^2 Q_{2\text{-D}}^* \left\{\frac{3.19 + 0.65\gamma + 4.3\gamma^2}{(1-\gamma^2)^{5/2}}\right\}, \quad (28)$$

and

$$(T_{base}^*)_{3\text{-D}} = 12\pi\mu R\gamma^2 Q_{2\text{-D}}{}^* \left\{\frac{1.15 + 0.70\gamma}{(1-\gamma^2)^{5/2}}\right\}.$$

These formulae are accurate for $\gamma < 0.8$. For larger γ, the lubrication approximations given in the Appendix should be used. In these calculations, the immersed cell has dimension R, $\gamma = R/H$ is the ratio of cell to channel width, and $Q_{2\text{-D}}^*$ is the flow rate per unit width in the system. Based upon comparisons with 3-D studies by Brooks and Tozeren (1996) and Pozrikidis (1997), these predictions for flow in a planar geometry are accurate to ~10%, and thus can be used to simply calculate the mechanical influence of fluid flow on an adherent cell in a flow chamber. By comparing our results to those of Chapman and Cokelet (1996), we expect that in circular geometries the relationships in Eq. 28 are accurate to within ~25% when $\gamma \ge 0.5$.

Finally, it is important to recognize that this is a model study with many simplifications. Although we expect that the predictions given here are accurate for rigid models of cells, they ignore the influence of cell deformability and cell-to-cell interaction, which could clearly alter the behavior predicted in this study. The methods described herein are readily adapted for investigations of these more complicated systems. Future investigations of the influence of deformability and interactions between cells could use the present study for comparison, to define the relative importance of these aspects for cell adhesion phenomena.

APPENDIX

This appendix provides a basic background for the computational and analytical approaches used in this study.

Boundary element method

The computational solution to the boundary value problem posed in the section on model development is challenging because the domain changes as a function of the extent of cell coverage. Conventional finite-difference techniques are difficult to implement because of the need to continually remesh the domain with changes in the number of aggregated cells. Biofilm models have been developed using the immersed boundary method to follow individual cells in a microchannel (Dillon et al., 1995, 1996). In the present model, however, we base our calculations on the boundary integral representation of Stokes flow, derived by Ladyzhenskaya (1963). The solution for the velocity field resulting from Stokes flow is obtained in terms of single- and double-layer potentials by taking Fourier transforms of Eq. 5 and applying Green's theorem (Ladyzhenskaya, 1963), which creates an integral relationship that must be satisfied:

$$\mathbf{u}_k(\mathbf{x}) = \int_S \mathbf{T}_{ik}(\mathbf{x}, \mathbf{y})\mathbf{u}_i dS_y - \frac{8}{\beta^2}\int_S \mathbf{U}_{ik}(\mathbf{x}, \mathbf{y})\boldsymbol{\tau}_i dS_y, \quad (29)$$

where

$$\mathbf{U}_{ik}(\mathbf{x}, \mathbf{y}) = -\frac{1}{4\pi}\left\{\delta_{ik}\log\left|\mathbf{x}-\mathbf{y}\right| - \frac{(x_i - y_i)(x_k - y_k)}{|\mathbf{x}-\mathbf{y}|^2}\right\},$$

$$\mathbf{T}_{ik}(\mathbf{x}, \mathbf{y}) = -\frac{1}{\pi}\frac{(x_i - y_i)(x_j - y_j)(x_k - y_k)}{|\mathbf{x}-\mathbf{y}|^4} n_j(\mathbf{y}). \quad (30)$$

Here S represents the boundary surface, and $\boldsymbol{\tau}_i = \sigma_{ij} n_j$, with i, j equal to 1 ($x$ direction) or 2 (y direction). As $\mathbf{x}$ approaches a point on the boundary surface, the solution of Eq. 29 becomes

$$\mathbf{C}_{ki}\mathbf{u}_i(\mathbf{x}) = \int_S \mathbf{T}_{ik}(\mathbf{x}, \mathbf{y})\mathbf{u}_i dS_y - \frac{8}{\beta^2}\int_S \mathbf{U}_{ik}(\mathbf{x}, \mathbf{y})\boldsymbol{\tau}_i dS_y, \quad (31)$$

where $\mathbf{x} \in S$, and the tensor $\mathbf{C}_{ki}$ accounts for stress discontinuities at the surface. $\mathbf{C}_{ki} = \frac{1}{2}\delta_{ki}$ if the boundary is smooth, but has a more complicated structure if the domain has corners (Brebbia and Dominguez, 1989).

Equation 29 is solved numerically by discretizing the boundary into N 3-point (quadratic) elements, so that

$$\mathbf{C}_{ki}\mathbf{u}_i(\mathbf{x}) - \sum_{j=1}^{N}\int_{S_j} \mathbf{T}_{ik}(\mathbf{x}, \mathbf{y})\mathbf{u}_i dS_y = -\frac{8}{\beta^2}\sum_{j=1}^{N}\int_{S_j} \mathbf{U}_{ik}(\mathbf{x}, \mathbf{y})\boldsymbol{\tau}_i dS_y, \quad (32)$$

where $\mathbf{u}$ and $\boldsymbol{\tau}$ are discretized along the domain and are represented by quadratic polynomials.

Equation 32 is represented by a system of linear equations,

$$\mathbf{Hw} = \mathbf{Gt}, \quad (33)$$

where $\mathbf{H}$ and $\mathbf{G}$ are, respectively, $4N \times 4N$ and $4N \times 6N$ matrices, and $w_{2j-1} = u_j$, $w_{2j} = v_j$, $t_{2j-1} = \tau_{xj}$, $t_{2j} = \tau_{yj}$ for $j = 1, \ldots, 2N$. Matrix $\mathbf{G}$ is made larger than $\mathbf{H}$ to allow the stress vector to have two distinct values at corner points because of two possible orientations of the normal vector. This is particularly useful at corner points, where stress discontinuities exist as a result of discontinuities in the normal vector. The elements of $\mathbf{H}$ and $\mathbf{G}$ are computed using a 10-point regular Gaussian quadrature if $\mathbf{x}$ does not coincide with one of the node points of S_j. Otherwise a 10-point logarithmic quadrature is used to evaluate those portions of the integrals in Eq. 31 that contain the logarithmic singularity. The diagonal coefficients of $\mathbf{H}$ are computed indirectly by imposing a uniform flow in both the x and y directions. We then apply the boundary conditions and rearrange the system so that $\mathbf{Az} = \mathbf{f}$, where $\mathbf{A}$ is a $4N \times 4N$ matrix, $\mathbf{z}$ is a $2N$ vector containing the unknown velocities and stresses, and $\mathbf{f}$ contains the known stress or velocity information. This system is solved using Gaussian elimination with partial pivoting. We have validated this technique in different systems, including those of Gaver et al. (1996) and Halpern and Gaver (1994).

Lubrication theory

In this section we derive lubrication approximations of the flow field through a channel with a single-cell protuberance on the bottom wall. In these calculations, we follow lubrication analysis of creeping flows. For details of this type of analysis, the reader is referred to Leal (1992). In the description that follows, we assume that $\partial^2 u/\partial y^2 \gg \partial^2 u/\partial x^2$ and $\partial P/\partial y \approx 0$, so that Eq. 5 is approximately

$$\frac{dP}{dx} = \frac{\beta^2}{8}\frac{\partial^2 u}{\partial y^2}, \quad (34)$$

with $\mathbf{u}(y = h_1(x)) = \mathbf{u}(y = h_2(x)) = 0$, to satisfy no slip on the top and bottom walls, respectively. From this and continuity (Eq. 5), the velocity field is

$$u(x, y) = A(x)y^2 + B(x)y + C(x)$$

and

$$v(x, y) = \frac{A'(x)}{3}y^3 - \frac{B'(x)}{2}y^2 - C'(x)y + D(x), \quad (35)$$

where

$$A(x) = \frac{4}{\beta^2}\frac{dP}{dx}, \quad B(x) = -\frac{4}{\beta^2}\frac{dP}{dx}(h_1(x) + h_2(x)),$$

$$C(x) = \frac{4}{\beta^2}\frac{dP}{dx}h_1(x)h_2(x)$$

and

$$D(x) = \frac{A'(x)}{3}h_2(x)^3 + \frac{B'(x)}{2}h_2(x)^2 + C'(x)h_2(x).$$

To satisfy Eq. 6, the local pressure gradient is

$$\frac{dP}{dx} = -\left[(h_1(x) - h_2(x))^3\int_{x=0}^{x=1}\frac{dx}{(h_1(x) - h_2(x))^3}\right]^{-1}. \quad (36)$$

From this result,

$$Q = \frac{2}{3\beta^2}\left[\int_{x=0}^{x=1}\frac{dx}{(h_1(x) - h_2(x))^3}\right]^{-1}. \quad (37)$$

From this, the shear-stress on the wall of a flat-walled channel is $(\tau_s)_{\text{flat-wall}} = \beta/2$, and the flow through a flat-walled channel is $Q_{\text{flat-wall}} = 2\beta/3$. Flow rate predictions from this analysis are provided by Eq. 20 and are demonstrated in Fig. 9.

Maximum shear stress

Given a semicircular protuberance of height $\gamma = R/H$, the lubrication theory calculation shows that the maximum shear stress is

$$\lim_{\gamma\to 1}\left(\frac{(\tilde{\tau}_s)_{\max}}{\tilde{Q}}\right) = \frac{1}{(1-\gamma)^2}. \quad (38)$$

x component of force, F_x

From lubrication theory in the limit of small gap width ($\gamma \to 1$),

$$\frac{\partial u}{\partial y} \gg \left(\frac{\partial u}{\partial x}, \frac{\partial v}{\partial x}, \frac{\partial v}{\partial y}\right),$$

the x component of the cell stress is

$$\tau_x = -P\cos\theta + \frac{\beta^2}{8}\frac{\partial u}{\partial y}\sin\theta.$$

Integrating over the surface of the cell,

$$\lim_{\gamma\to 1}\left(\frac{\tilde{F}_x}{\tilde{Q}}\right) = \frac{2\pi}{(1-\gamma^2)^{5/2}}. \quad (39)$$

Torque

The cell shear-stress is

$$\tau_s = -\frac{\beta^2}{2}\frac{\partial v}{\partial y}(\sin\theta\cos\theta) + \frac{\beta^2}{8}\left(\frac{\partial u}{\partial y} + \frac{\partial v}{\partial x}\right)(\sin^2\theta - \cos^2\theta).$$

In the limit of small gap width ($\gamma \to 1$), using Eq. 18,

$$\lim_{\gamma\to 1}\left(\frac{\tilde{T}_{base}}{\tilde{Q}}\right) = \frac{2}{(1-\gamma^2)^{5/2}}. \quad (40)$$

These results are used above (see Regression Relationships) to develop regression formulae.

This work was funded in part by DoE grant FG-01-93EW53023, National Science Foundation National Young Investigator Award BCS-9358207, and National Institutes of Health grant HL51334, and National Science Foundation Group Infrastructure Award DMS-97-09754.

REFERENCES

Barbee, K. A., T. Mundel, R. Lal, and P. F. Davies. 1995. Subcellular distribution of shear stress at the surface of flow-aligned and nonaligned endothelial monolayers. *Am. J. Physiol.* 268:H1765–H1772.

Berg, H. C., and L. Turner. 1990. Chemotaxis of bacteria in glass capillary arrays. *Biophys. J.* 58:919–930.

Brebbia, C. A., and J. Dominguez. 1989. Boundary Elements—An Introductory Course. Computational Mechanics, Southampton, England.

Brooks, S. B., and A. Tozeren. 1996. Flow past an array of cells that are adherent to the bottom plate of a flow channel. *Computers Fluids.* 25:741–757.

Chapman, G., and G. Cokelet. 1996. Model studies of leukocyte-endothelium-blood interactions. I. The fluid flow drag force on the adherent leukocyte. *Biorheology.* 33:119–138.

Chapman, G. B., and G. R. Cokelet. 1997. Model studies of leukocyte-endothelium-blood interactions. II. Hemodynamic impact of leukocyte adherent to the wall of post-capillary vessels. *Biorheology.* 32:37–56.

Characklis, W. G., and K. C. Marshall. 1990. Biofilms: A Basis for an Interdisciplinary Approach. John Wiley and Sons, New York.

Davies, P. F. 1995. Flow-mediated endothelial mechanotransduction. *Physiol. Rev.* 75:519–560.

Dillon, R., L. Fauci, A. Fogelson, and D. P. Gaver. 1996. Modeling biofilm processes using the immersed boundary method. *J. Comput. Phys.* 129:57–73.

Dillon, R., L. Fauci, and D. Gaver. 1995. A microscale model of bacterial swimming, chemotaxis and substrate transport. *J. Theor. Biol.* 177: 325–340.

Fung, Y. C. 1984. Biodynamics: Circulation. Springer-Verlag, New York.

Gaver, D. P., III, D. Halpern, O. E. Jensen, and J. B. Grotberg. 1996. The steady motion of a semi-infinite bubble through a flexible-walled channel. *J. Fluid Mech.* 319:25–65.

Goetz, D. J., M. E. El-Sabban, B. U. Pauli, and D. A. Hammer. 1994. Dynamics of neutrophil rolling over stimulated endothelium in vitro. *Biophys. J.* 66:2202–2209.

Halpern, D., and D. P. Gaver, III. 1994. Boundary element analysis of the time-dependent motion of a semi-infinite bubble in a channel. *J. Comput. Phys.* 115:366–375.

Hammer, D. A., and S. M. Apte. 1992. Simulation of cell rolling and adhesion on surfaces in shear flow: general results and analysis of selectin-mediated neutrophil adhesion. *Biophys. J.* 63:35–57.

Harkes, G., J. Dankert, and J. Feijen. 1992. Bacterial migration along solid surfaces. *Appl. Environ. Microbiol.* 58:1500–1505.

Higdon, J. J. L. 1985. Stokes flow in arbitrary two-dimensional domains: shear flow over ridges and cavities. *J. Fluid Mech.* 159:195–226.

Horsfield, K., and W. I. Gordon. 1981. Morphology of pulmonary veins in man. *Lung.* 159:211–218.

Ingber, D. E. 1997. Tensegrity, the architectural basis of cellular mechanotransduction. *Annu. Rev. Physiol.* 59:575–599.

Konstantopoulos, K., and L. V. McIntire. 1996. Cell adhesion in vascular biology. *J. Clin. Invest.* 98:2661–2665.

Ladyzhenskaya, O. A. 1963. The Mathematical Theory of Viscous Incompressible Flow. Gordon and Breach, New York.

Leal, L. G. 1992. Laminar Flow and Convective Transport Processes: Scaling Principles and Asymptotic Analysis. Butterworth-Heinemann, Boston.

Olivier, L. A., and G. A. Truskey. 1993. A numerical analysis of forces exerted on spreading cells in a parallel plate flow chamber assay. *Biotechnol. Bioeng.* 42:963–973.

Pozrikidis, C. 1997. Shear flow over a protuberance on a plane wall. *J. Eng. Math.* 31:29–42.

Schmid-Schoenbein, G. W., Y. C. Fung, and B. Zeifach. 1975. Vascular endothelium-leukocyte interaction: sticking shear force in venules. *Circ. Res.* 36:173–184.

Tempelman, L. A., and D. A. Hammer. 1994. Receptor-mediated binding of IgE-sensitized rat basophilic leukemia cells to antigen-coated substrates under hydrodynamic flow. *Biophys. J.* 66:1231–1243.